

# TiS<sub>3</sub> nanoribbons: Width-independent band gap and strain-tunable electronic properties

Jun Kang,<sup>1,\*</sup> Hasan Sahin,<sup>1</sup> H. Duygu Ozaydin,<sup>2</sup> R. Tugrul Senger,<sup>2</sup> and François M. Peeters<sup>1</sup>

<sup>1</sup>Department of Physics, University of Antwerp, Groenenborgerlaan 171, BE-2020 Antwerpen, Belgium

<sup>2</sup>Department of Physics, Izmir Institute of Technology, 35430 Izmir, Turkey

(Received 27 April 2015; published 10 August 2015)

The electronic properties, carrier mobility, and strain response of TiS<sub>3</sub> nanoribbons (TiS<sub>3</sub> NRs) are investigated by first-principles calculations. We found that the electronic properties of TiS<sub>3</sub> NRs strongly depend on the edge type (**a** or **b**). All **a**-TiS<sub>3</sub> NRs are metallic with a magnetic ground state, while **b**-TiS<sub>3</sub> NRs are direct band gap semiconductors. Interestingly, the size of the band gap and the band edge position are almost independent of the ribbon width. This feature promises a constant band gap in a **b**-TiS<sub>3</sub> NR with rough edges, where the ribbon width differs in different regions. The maximum carrier mobility of **b**-TiS<sub>3</sub> NRs is calculated by using the deformation potential theory combined with the effective mass approximation and is found to be of the order 10<sup>3</sup> cm<sup>2</sup> V<sup>-1</sup> s<sup>-1</sup>. The hole mobility of the **b**-TiS<sub>3</sub> NRs is one order of magnitude lower, but it is enhanced compared to the monolayer case due to the reduction in hole effective mass. The band gap and the band edge position of **b**-TiS<sub>3</sub> NRs are quite sensitive to applied strain. In addition we investigate the termination of ribbon edges by hydrogen atoms. Upon edge passivation, the metallic and magnetic features of **a**-TiS<sub>3</sub> NRs remain unchanged, while the band gap of **b**-TiS<sub>3</sub> NRs is increased significantly. The robust metallic and ferromagnetic nature of **a**-TiS<sub>3</sub> NRs is an essential feature for spintronic device applications. The direct, width-independent, and strain-tunable band gap, as well as the high carrier mobility, of **b**-TiS<sub>3</sub> NRs is of potential importance in many fields of nanoelectronics, such as field-effect devices, optoelectronic applications, and strain sensors.

DOI: 10.1103/PhysRevB.92.075413

PACS number(s): 73.22.-f, 75.75.-c, 72.20.Fr

## I. INTRODUCTION

The successful isolation of graphene [1] in 2004 stimulated a lot of research interest on two-dimensional (2D) materials with atomic thickness. With the rapidly developed techniques of atomic-scale-thick crystal synthesis and characterization, more and more members have joined the family of 2D materials, such as BN [2], silicene [3], germanane [4], GaS [5], and phosphorene [6]. Among them transition-metal chalcogenides (TMCs) have particularly attracted considerable attention owing to their extraordinary fundamental physical properties and their application potential in electronic devices. The most well known member of the TMC family is MoS<sub>2</sub>. It was shown that single-layer MoS<sub>2</sub> is a direct band gap semiconductor [7], and it is regarded as a promising material for a field-effect transistor with a high on/off ratio [8]. There are also various studies of MoS<sub>2</sub> in relation to its light emission [9], strain response [10,11], excitonic effects [12], valley polarization [13], and photoresponsivity [14]. Other TMCs also possess many interesting properties. For example, multilayer MoSe<sub>2</sub> shows thermally driven enhancement in photoluminescence [15], and bulk ReS<sub>2</sub> behaves as electronically and vibrationally decoupled monolayers stacked together [16,17].

In addition, several recent works have reported the synthesis of thin TiS<sub>3</sub> films and few-layer TiS<sub>3</sub> nanoribbons (TiS<sub>3</sub> NRs) [18–21]. The TiS<sub>3</sub> nanostructures exhibit a direct band gap of 1.1–1.2 eV, which may be interesting for possible replacement of Si in applications when high gain is needed [20]. The elastic modulus and carrier mobility of TiS<sub>3</sub> are strongly anisotropic, and monolayer TiS<sub>3</sub> is predicted to have a high electron mobility [22]. More importantly, the fabricated TiS<sub>3</sub> NRs show ultrahigh photoresponse and fast switching times [20].

These features are highly desirable for photodetection and photovoltaic applications.

Although there are a few theoretical investigations on the electronic properties of two-dimensional TiS<sub>3</sub> [22–24], the characteristic properties of one-dimensional nanoscale structures of TiS<sub>3</sub> (TiS<sub>3</sub> NRs) have not been explored. Our study addresses some important questions on this novel material: (i) Do TiS<sub>3</sub> NRs show chirality-dependent electronic and magnetic properties like graphene [25] and MoS<sub>2</sub> [26] NRs? (ii) Does quantum confinement in one dimension result in a width-dependent electronic band gap of TiS<sub>3</sub> NRs as in NRs of graphene [25], graphane [27], silicene [28], and phosphorene [29]? (iii) What is the role of applied strain, which was shown to tune the electronic properties of chalcogenides [10,11], in the properties of TiS<sub>3</sub> NRs? (iv) Can the high electron mobility predicted for TiS<sub>3</sub> [22] be preserved in the NRs? (v) How are the properties of the TiS<sub>3</sub> NRs affected by edge passivation?

In this work we address the above-mentioned questions using state-of-the-art *ab initio* calculations. This paper is organized as follows: First, we briefly introduce the computational method in Sec. II. Then we discuss structural and energetic properties of TiS<sub>3</sub> NRs in Sec. III. The band structure, magnetic properties, and the dependence of the band gap on the ribbon width are investigated in Sec. IV. Next, in Sec. V we investigate the effects of strain on the band structure of TiS<sub>3</sub> NRs. We study the mobility of TiS<sub>3</sub> NRs using the deformation potential theory in combination with the effective mass approximation in Sec. VI. Finally, the effects of hydrogen passivation on TiS<sub>3</sub> NRs are discussed in Sec. VII. The results are concluded in Sec. VIII.

## II. COMPUTATIONAL METHODS

All the calculations are carried out using the Vienna *Ab initio* Simulation Package (VASP) [30,31]. The frozen-core

\*jun.kang@uantwerpen.be

projector augmented wave (PAW) method [32] and the generalized gradient approximation of Perdew-Burke-Ernzerhof (GGA-PBE) [33] are adopted. The wave functions are expanded in a plane-wave basis set with a cutoff of 400 eV. Brillouin zone sampling is performed with the Monkhorst-Pack (MP) special  $k$ -point meshes [34] including the  $\Gamma$  point. The  $k$  grid for nanoribbons is either  $7 \times 1 \times 1$  or  $1 \times 11 \times 1$ , depending on the ribbon orientation, and for a monolayer a  $7 \times 11 \times 1$  grid is used. The vacuum layer is larger than 10 Å between two adjacent images. The convergence threshold for structure relaxation is 0.01 eV/Å. The vacuum level is taken as the zero reference, which is used to align the energy in different ribbons and to calculate the deformation potential. Part of the calculations is also performed using the Heyd-Scuseria-Ernzerhof (HSE06) hybrid functional [35,36] to get better band gap values. By mixing the PBE and Hartree-Fock (HF) exchange functionals together, the HSE06 method reduces the localization and delocalization errors [37] of those functionals and describes the band gap much better. The screening length of HSE06 is 0.2 Å<sup>-1</sup>, and the mixing rate of the HF exchange potential is 0.25.

### III. STRUCTURAL PROPERTIES AND EDGE ENERGETICS

The monolayer TiS<sub>3</sub> has a rectangle unit cell with two lattice vectors,  $a$  and  $b$ . Our optimized values for  $a$  and  $b$  are 3.41 and 5.02 Å, respectively, which are very close to the experimental bulk values (3.40 and 4.96 Å) [38] and other theoretical results (3.39 and 4.98 Å) [23]. In the present work, two types of ribbons are studied, with their ribbon axis along the  $a$  and  $b$  axes. The nanoribbons are indicated as  $N\text{-a-TiS}_3$  NR and  $N\text{-b-TiS}_3$  NR, where  $N$  stands for the number of Ti atoms in the unit cell of the ribbon and **a**-TiS<sub>3</sub> NR and **b**-TiS<sub>3</sub> NR are along the  $a$  and  $b$  lattice vectors, respectively. Here we consider  $N = 6\text{--}12$  for **a**-TiS<sub>3</sub> NR and  $N = 4\text{--}10$  for **b**-TiS<sub>3</sub> NR. Figures 1(a) and 1(c) show the structure of 8-a-TiS<sub>3</sub> NR and 6-b-TiS<sub>3</sub> NR. In Figs. 1(b) and 1(d) variation of the edge energy with ribbon width is shown. The edge energy of an  $N$ -TiS<sub>3</sub> NR is defined as  $(E_{\text{NR}} - \frac{N}{2}E_{2\text{D}})/(2L)$ , where  $E_{\text{NR}}$  is the total energy of the ribbon unit cell,  $E_{2\text{D}}$  is the total energy of a primitive unit cell of a TiS<sub>3</sub> monolayer, and  $L$  is the lattice constant along the axis of the ribbon. The edge energy describes the energy cost to create a new edge from a monolayer. The edge energy of **a**-TiS<sub>3</sub> NRs oscillates with different ribbon widths and ranges from 454 to 475 meV/Å. This is close to the values of many other TMC nanoribbons such as ribbons of MoS<sub>2</sub>, WS<sub>2</sub>, and ZrS<sub>2</sub> [39]. The situation in **b**-TiS<sub>3</sub> NRs is, however, much different; the edge energy is typically around 60 meV/Å and slightly decreases as the ribbon width increases. Compared with the edge energies of graphene and many other TMC nanoribbons, which are on the order of 1 eV/Å [39,40], **b**-TiS<sub>3</sub> NRs have much lower edge energy, suggesting that formation of **b**-TiS<sub>3</sub> NRs from 2D TiS<sub>3</sub> could be much easier. In fact, the experimentally reported TiS<sub>3</sub> NRs are along the  $b$  direction [20]. The low edge energy of **b**-TiS<sub>3</sub> NRs can be attributed to the fact that the bonds along the  $a$  direction in 2D TiS<sub>3</sub> are much weaker than those along  $b$ , in accordance with the low in-plane stiffness (5.225 eV/Å<sup>2</sup>) along this direction.

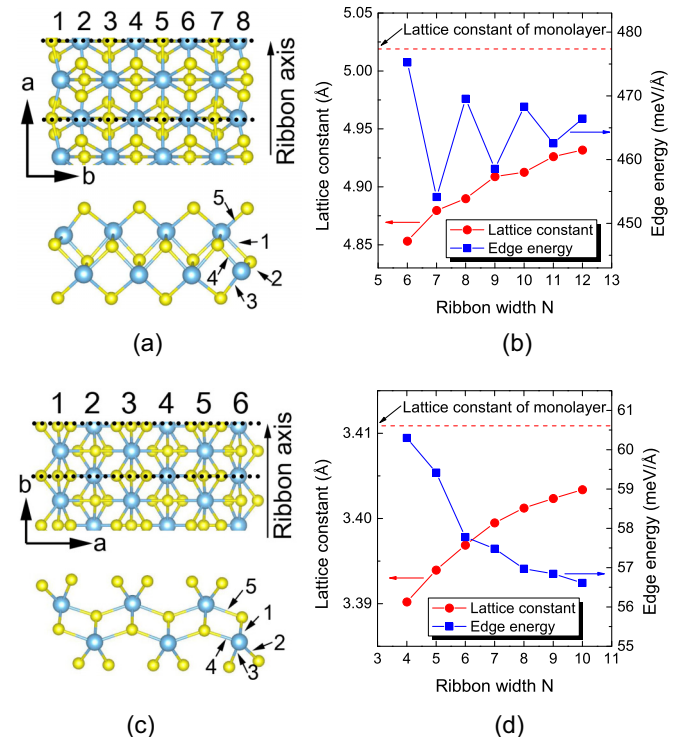


FIG. 1. (Color online) (a) Top view and side view of an 8-a-TiS<sub>3</sub> NR.  $a$  and  $b$  are the lattice vectors of the 2D TiS<sub>3</sub>. The dashed lines indicate the unit cell of the 8-a-TiS<sub>3</sub> NR. The bonds at the edge are labeled 1–5. (b) The lattice constant and edge energy of different a-TiS<sub>3</sub> NRs. The red dashed line indicates the lattice constant along  $a$  of the 2D TiS<sub>3</sub>. (c) The same as (a), but for a 6-b-TiS<sub>3</sub> NR. (d) The same as (b), but for 6-b-TiS<sub>3</sub> NRs.

In the TiS<sub>3</sub> NRs, there is no remarkable structural reconstruction, and the overall geometry of the monolayer is maintained. Due to the dangling bonds at the edge, the edge atoms undergo a structural relaxation. The lengths of the different bonds at the edges for the 8-a-TiS<sub>3</sub> NR and 6-b-TiS<sub>3</sub> NR are listed in Table I. Compared with the case of the monolayer, in 8-a-TiS<sub>3</sub> NR the length of bond 1 becomes larger, but the other bonds become shorter. In 6-b-TiS<sub>3</sub> NR, the lengths of bonds 2 and 3 slightly increase, whereas the lengths of bonds 1, 4, and 5 decrease significantly. Therefore, in general the bonds at the edge exhibit a contractive behavior. Apparently, the dangling bonds that originate from the edge atoms result in compressive edge stress. To further understand the reorganization of edge atoms we also calculate the edge stresses of different TiS<sub>3</sub> NRs using the method in Ref. [38].

TABLE I. The length of the edge bonds of an 8-a-TiS<sub>3</sub> NR and a 6-b-TiS<sub>3</sub> NR and the corresponding values in a TiS<sub>3</sub> monolayer. The labels of the bonds are shown in Fig. 1.

Bond index	1	2	3	4	5
Bonds in a-TiS <sub>3</sub> NR (Å)	2.62	2.57	2.38	2.23	2.43
Bonds in monolayer (Å)	2.46	2.67	2.50	2.46	2.50
Bonds in b-TiS <sub>3</sub> NR (Å)	2.40	2.52	2.51	2.50	2.61
Bonds in monolayer (Å)	2.46	2.50	2.50	2.67	2.67

For **a**-TiS<sub>3</sub> NRs, the edge stress is in the range of 3.19–5.07 eV/Å. For **b**-TiS<sub>3</sub> NRs, when  $N$  goes from 4 to 10, the edge stress decreases from 0.19 to 0.17 eV/Å. The edge stress of **a**-TiS<sub>3</sub> NRs is much larger than that of **b**-TiS<sub>3</sub> NRs, which can be attributed to the larger bond contraction at the edges of **a**-TiS<sub>3</sub> NR. The compressive edge stress also reduces the lattice constants of the TiS<sub>3</sub> NRs. As seen in Figs. 1(b) and 1(d), the lattice constants of TiS<sub>3</sub> NRs are smaller than the value of the 2D monolayer. This behavior is more significant in **a**-TiS<sub>3</sub> NRs because of their larger edge stress. As the width of the ribbon increases, the lattice constant becomes closer to that of the 2D monolayer.

#### IV. WIDTH-DEPENDENT ELECTRONIC STRUCTURE

We next study the electronic structure and width-dependent characteristics of **a**- and **b**-TiS<sub>3</sub> NRs. Our calculations reveal that all the **a**-TiS<sub>3</sub> NRs have metallic characters with nonzero density of states at the Fermi level. The electronic band dispersion of 10-**a**-TiS<sub>3</sub> NR, which is representative of all **a**-TiS<sub>3</sub> NRs, is shown in Fig. 2(a). It is seen from the figure that the metallic property stems from multiple up and down bands crossing the Fermi level at different points of the Brillouin zone. Another feature of **a**-TiS<sub>3</sub> NRs is their magnetic ground state. We see that for various ribbon widths spin polarization results in a net magnetic moment varying between  $0.2\mu_B$  and  $0.8\mu_B$  per unit cell. To get further insight into the spin polarization in **a**-TiS<sub>3</sub> NRs, we also calculate the spin density, which is the difference between up and down spin channels, for the 10-**a**-TiS<sub>3</sub> NR. As shown in Fig. 2(b), while the spin-polarized state mainly originates from the unpaired electrons of edge atoms, there is a small (ignorable) contribution from the Ti (S) atoms inside the ribbon.

In contrast to the **a**-TiS<sub>3</sub> NRs, all **b**-TiS<sub>3</sub> NRs are found to have a direct band gap located at the  $\Gamma$  point. In addition, magnetic structure analysis reveals that the **b**-TiS<sub>3</sub> NRs have no ferromagnetic or antiferromagnetic order in their ground state, and therefore, they are nonmagnetic semiconductors. In Fig. 3(a) a representative band structure of **b**-TiS<sub>3</sub> NRs (for

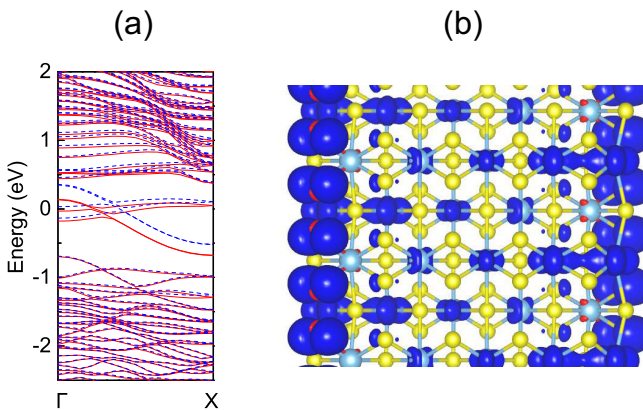


FIG. 2. (Color online) (a) The band structures of a 10-**a**-TiS<sub>3</sub> NR obtained by GGA-PBE. Spin-up and spin-down channels are presented by red solid and blue dashed curves, respectively. The Fermi level is set to zero. (b) The magnetization charge density of the 10-**a**-TiS<sub>3</sub> NR.

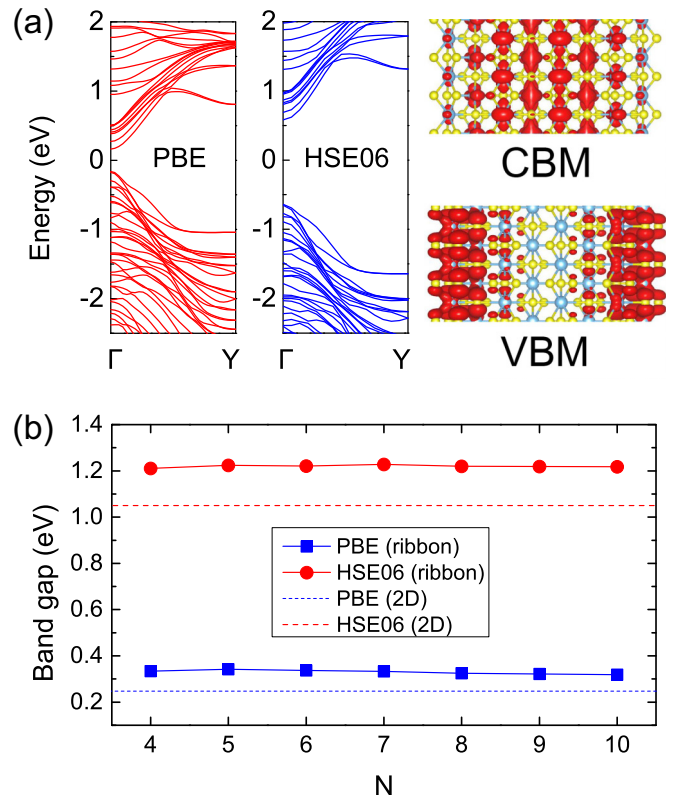


FIG. 3. (Color online) (a) The band structures of an 8-**b**-TiS<sub>3</sub> NR obtained by GGA-PBE and HSE06 and the charge density of its CBM and VBM states. (b) The band gap as a function of the **b**-TiS<sub>3</sub> NR width  $N$ . Both GGA-PBE and HSE06 results are given. The dashed lines are the values for the 2D case.

8-**b**-TiS<sub>3</sub> NR) is presented. It is seen that 8-**b**-TiS<sub>3</sub> NRs have a band gap of 0.32 eV. However, the HSE06-approximated band gap value is 1.22 eV. It is well known that although the band dispersions are almost the same in bare-GGA and HSE06 calculations, band gap values are underestimated by GGA exchange-correlation functionals. Therefore, we show band gap values of HSE06 together with GGA-PBE in Fig. 3. If not specified, the results in the following are from GGA-PBE. In Fig. 3(a), the charge densities of conduction-band minimum (CBM) and valence-band maximum (VBM) states are plotted. The VBM state is localized at the edges and is mainly composed of the S  $p_y$  orbital, together with some contributions from the Ti  $d_{xy}$  and  $d_{yz}$  orbitals ( $x$  and  $y$  are along the transverse and axial directions of **b**-TiS<sub>3</sub> NRs, respectively, and  $z$  is perpendicular to the ribbon plane). On the other hand, the CBM state is distributed inside the ribbon, and it mainly originates from Ti  $d_{x^2-y^2}$  and  $d_{z^2}$  orbitals.

The unique width dependence of the band gap values of **b**-TiS<sub>3</sub> NRs is illustrated in Fig. 3(b). Usually, due to the quantum confinement effect, the band gap of the nanoribbons is strongly width dependent [25,27–29]. As the width  $W$  of the ribbon increases, the band gap decreases and gradually approaches the monolayer limit, and the typical decay behavior is  $1/W^\alpha$ . However, for **b**-TiS<sub>3</sub> NRs, it is interesting to note that the band gap is almost independent of the ribbon width. All **b**-TiS<sub>3</sub> NRs exhibit direct gaps around 0.32 eV (GGA-PBE)

TABLE II. Calculated effective masses of holes ( $m_h^*$ ) and electrons ( $m_e^*$ ), deformation potential constants for VBM ( $E_v$ ) and CBM ( $E_c$ ), elastic moduli ( $C_{1D}$  and  $C_{2D}$ ), and carrier mobilities for holes and electrons ( $\mu_h$  and  $\mu_e$ ) at 300 K for a  $\text{TiS}_3$  monolayer and the **b**- $\text{TiS}_3$  NRs.  $m_0$  is the mass of a free electron.  $C_{1D}$  for **a**-ribbons is shown in Fig. 4.

	$m_h^*$ ( $m_0$ )	$m_e^*$ ( $m_0$ )	$E_v$ (eV)	$E_c$ (eV)	$C_{1D}$ (eV/ $\text{\AA}$ )	$C_{2D}$ (eV/ $\text{\AA}^2$ )	$\mu_h$ ( $10^3 \text{ cm}^2 \text{ V}^{-1} \text{ s}^{-1}$ )	$\mu_e$ ( $10^3 \text{ cm}^2 \text{ V}^{-1} \text{ s}^{-1}$ )
Monolayer (along <i>a</i> )	0.308	1.523	3.882	0.740		5.225	0.831	0.935
Monolayer (along <i>b</i> )	0.998	0.381	-4.443	0.780		8.373	0.097	21.611
$N = 4$	0.160	0.361	-7.969	1.339	85.788		0.168	1.751
$N = 5$	0.163	0.362	-8.107	1.437	106.955		0.196	1.885
$N = 6$	0.165	0.369	-8.134	1.485	128.059		0.229	2.057
$N = 7$	0.204	0.370	-8.046	1.533	148.375		0.197	2.228
$N = 8$	0.202	0.374	-8.224	1.386	170.233		0.219	3.092
$N = 9$	0.204	0.373	-8.112	1.362	190.133		0.248	3.576
$N = 10$	0.206	0.374	-8.200	1.311	209.585		0.264	4.222

or 1.22 eV (HSE06). Furthermore, for  $N > 5$ , the positions of CBM and VBM states in different **b**- $\text{TiS}_3$  NRs are nearly the same; the difference is only a few meV. Therefore, the band offset between ribbons of different widths is almost zero.

The reason for the width-independent band gap can be explored by further analyzing the character of the VBM and CBM states. As shown in Fig. 3(a), the VBM states of **b**- $\text{TiS}_3$  NRs originate from the edge states, and charge carriers are negligibly confined along the *a* direction; hence, the VBM energy has a weak width dependence. On the other hand, the CBM states are mainly composed of the inner region and hence are more “bulklike” than the VBM states and can be affected by the quantum confinement effect. The strength of quantum confinement is inversely proportional to the effective mass [41]. The electron effective mass of 2D  $\text{TiS}_3$  along the *a* direction is quite large ( $1.52m_0$ ; see Table II), indicating a quite flat conductive band along this direction. As a result, the confinement along the *a* direction introduces only minor changes of the CBM states. Therefore, the positions of VBM and CBM are not significantly affected by the confinement along *a*, leading to a width-independent band gap.

Synthesis of ribbons in laboratory conditions is always realized together with the formation of edge roughnesses which lead to undesired fluctuations in electronic properties of the structure. We see that for **b**- $\text{TiS}_3$  NRs, for a wide range of ribbon width, the band gap is almost constant and the band offset is negligible. Even with rough edges, the band gap of **b**- $\text{TiS}_3$  NR shows no spatial variation; also there is no transport barrier induced by a band offset. Such a property can facilitate the easy integration of **b**- $\text{TiS}_3$  NRs in electronic devices. In addition, compared with the monolayer case, the gaps of **b**- $\text{TiS}_3$  NRs are slightly larger. The gap value of 1.22 eV predicted by HSE06 is also good for adsorption of visible light, making **b**- $\text{TiS}_3$  NRs promising candidates for optoelectronic applications.

## V. MECHANICAL PROPERTIES AND RESPONSE TO STRAIN

The mechanical properties for 2D and one-dimensional (1D) materials can be characterized by their elastic moduli  $C_{2D}$  and  $C_{1D}$ . For a 2D system,  $C_{2D} = (1/S_0)(\partial^2 E / \partial \varepsilon^2)$ , where  $E$  is the total energy and  $S_0$  is the equilibrium area. For a 1D system,  $C_{1D} = (1/L)(\partial^2 E / \partial \varepsilon^2)$ , where  $L$  is the

lattice constant. The calculated results for different  $\text{TiS}_3$  NRs are shown in Fig. 4. The elastic modulus is found to scale linearly with the width. Moreover, with the same  $N$ , the width of an **a**- $\text{TiS}_3$  NR is larger than that of a **b**- $\text{TiS}_3$  NR, but the elastic modulus of the former is much smaller. Therefore, the strength of **a**- $\text{TiS}_3$  NRs is smaller than that of **b**- $\text{TiS}_3$  NRs. This is consistent with the smaller in-plane stiffness along the *a* direction in the  $\text{TiS}_3$  monolayer (see Table II).

Next, we investigate the band structure response of **b**- $\text{TiS}_3$  NRs to strain  $\varepsilon$  by applying uniaxial tensile strain up to 10%. The variation of the band gap with strain is plotted in Fig. 5(a). Notice that the band gap of **b**- $\text{TiS}_3$  NRs monotonously increases with increasing strain. The response of **b**- $\text{TiS}_3$  NRs with different widths is quite similar. The band gaps increase from  $\sim 0.3$  eV at  $\varepsilon = 0$  to  $\sim 0.9$  eV at  $\varepsilon = 10\%$ . Within the range of  $0\% < \varepsilon < 4\%$ , the changes in the band gap of different ribbons are almost identical. Even for  $\varepsilon$  up to 10%, at each strain value, the maximum difference in the band gap is less than 90 meV for  $N = 4\text{--}10$ . The band gap of 4-**b**- $\text{TiS}_3$  NR is still direct at  $\Gamma$  in the strain range considered. In other **b**- $\text{TiS}_3$  NRs, a direct-to-indirect band gap transition is observed when strain is sufficiently large. The threshold strain value of such a transition changes with the width of the ribbon. It is smaller in a wider ribbon. For example, the transition occurs at 10%, 6%, and 4% for  $N = 6, 8$ , and 10, respectively. Figure 5(b)

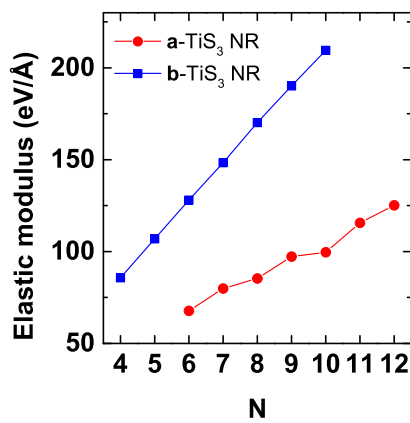


FIG. 4. (Color online) The calculated 1D elastic modulus for **a**- $\text{TiS}_3$  NRs and **b**- $\text{TiS}_3$  NRs as a function of the NR width.

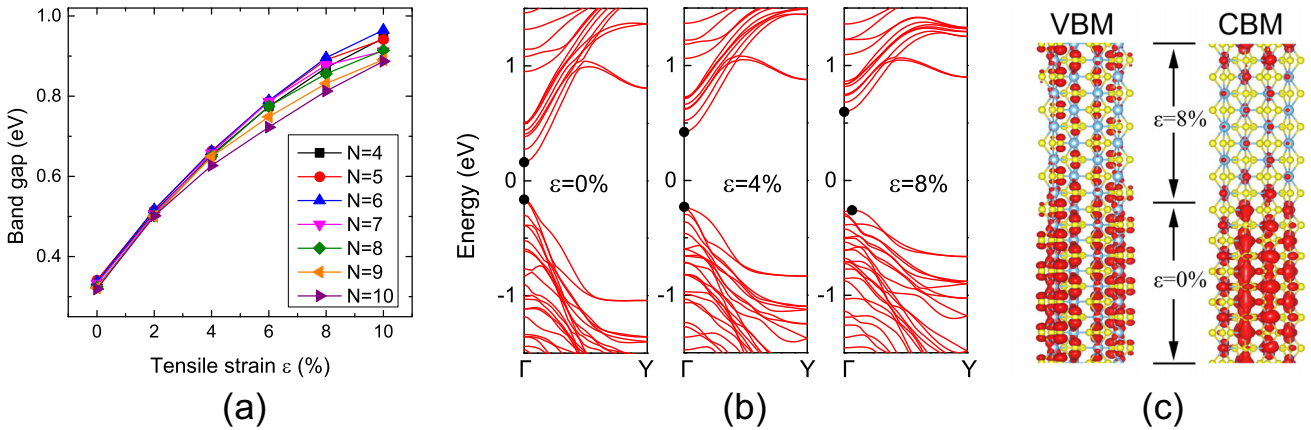


FIG. 5. (Color online) (a) The band gap of **b**-TiS<sub>3</sub> NRs as a function of tensile strain  $\varepsilon$ . (b) The band structure of an 8-**b**-TiS<sub>3</sub> NR with  $\varepsilon = 0\%$ ,  $4\%$ , and  $8\%$ . The dots indicate the CBM and VBM states. (c) The CBM and VBM charge density of a 4-**b**-TiS<sub>3</sub> NR which is locally strained by  $8\%$ .

shows the band structure of an 8-**b**-TiS<sub>3</sub> NR with different strains. At  $\varepsilon = 4\%$ , the band gap is direct. When  $\varepsilon$  is  $8\%$ , the VBM state moves a little away from the  $\Gamma$  point, while the CBM state remains at  $\Gamma$ , resulting in an indirect band gap. However, the direct gap at the  $\Gamma$  point is only 14 meV larger than the indirect gap. This is similar for other **b**-TiS<sub>3</sub> NRs. The difference between the direct and indirect gaps is very small, on the order of 10 meV. Also, the VBM state is still very close to the  $\Gamma$  point after the direct-to-indirect band gap transition. Hence, all the **b**-TiS<sub>3</sub> NRs can be considered to have direct or quasidirect band gap when tensile strain is applied.

The increase in band gap with increasing tensile strain is also consistent with the calculated deformation potential constant listed in Table II. The deformation potential constant, which is the measure of the energy shift of the band edge states with respect to strain, is defined by  $dE_{\text{edge}}/d\varepsilon$ , where  $E_{\text{edge}}$  is the band edge energy and  $\varepsilon$  is the applied strain. For **b**-TiS<sub>3</sub> NRs, the deformation potential is positive for CBM and negative for VBM. As a result, when tensile strain is applied, the CBM shifts upwards (energy increases), and the VBM shifts downwards (energy decreases), leading to a larger band gap. The calculated deformation potential also implies that the band alignment between unstrained and stretched **b**-TiS<sub>3</sub> NRs is type I. When tensile strain is applied to a segment of a **b**-TiS<sub>3</sub> NR, a type-I band offset can be formed. The CBM (VBM) of the strained region will be higher (lower) than that of the unstrained region. Consequently, electrons and holes will localize in the unstrained region. The localization enhances the combination rate of electrons and holes and thus can lead to a stronger photoluminescence. The calculated charge densities of the CBM and VBM states of 4-**b**-TiS<sub>3</sub> NR, shown in Fig. 5(c), with a local strain of  $8\%$  (one part of the ribbon is strained, and the other part is unstrained), show that both the CBM and VBM are mainly localized in the unstrained region. Except for carrier localization, local strain can also affect the charge transport properties of **b**-TiS<sub>3</sub> NRs. Enlargement of the band gap in the strained region induces energy barriers for electrons and holes in the ribbon, which can reduce the conductivity. Hence, the **b**-TiS<sub>3</sub> NRs can be potentially important as strain sensor.

## VI. CARRIER MOBILITY

Carrier mobility is a critical property of semiconductors. High mobility leads to a high response of carriers to an external field and therefore is feasible for high-speed field-effect devices. In this part we discuss the carrier mobility of **b**-TiS<sub>3</sub> NRs. A recent theoretical study reported that the carrier mobility in 2D monolayer TiS<sub>3</sub> is highly anisotropic, and the electron mobility along the *b* direction is of the order of  $10^4 \text{ cm}^2 \text{ V}^{-1} \text{ s}^{-1}$  [22]. The experimentally reported mobility of TiS<sub>3</sub> is of the order of  $10^2 \text{ cm}^2 \text{ V}^{-1} \text{ s}^{-1}$  for sheets and  $10^0 \text{ cm}^2 \text{ V}^{-1} \text{ s}^{-1}$  for ribbons [20,21]. The deviation between theoretical and experimental values stems from the fact that the TiS<sub>3</sub> materials in experiment are multilayers rather than a monolayer and that the presence of defects and a substrate in the experiment can affect the mobility to a large extent. Nevertheless, predicting mobility from theory provides valuable insight into the fundamental properties of materials. Recently, the anisotropic character of the carrier mobility in TiS<sub>3</sub> was also observed in an experimental study [21].

In inorganic semiconductors, one dominant mechanism of the scattering of carriers at low energy is the electron-acoustic phonon coupling, which can be well described by a deformation potential theory proposed by Bardeen and Shockley [42]. In combination with the effective mass approximation, the carrier mobility in 2D and 1D systems can be calculated by the following formulas [43–46]:

$$\mu_{2D} = \frac{2e\hbar^3 C_{2D}}{3k_B T |m^*|^2 |E_1|^2}, \quad (1)$$

$$\mu_{1D} = \frac{e\hbar^2 C_{1D}}{(2\pi k_B T)^{1/2} |m^*|^{3/2} |E_1|^2}. \quad (2)$$

Here  $k_B$  is the Boltzmann constant,  $T$  is the temperature, and  $m^*$  is the carrier effective mass.  $E_1$  is the deformation potential constant.  $C_{1D}$  and  $C_{2D}$  are the elastic moduli for 1D and 2D systems, respectively.

It was demonstrated that polar scattering can be an important factor in limiting the carrier mobility at high temperatures

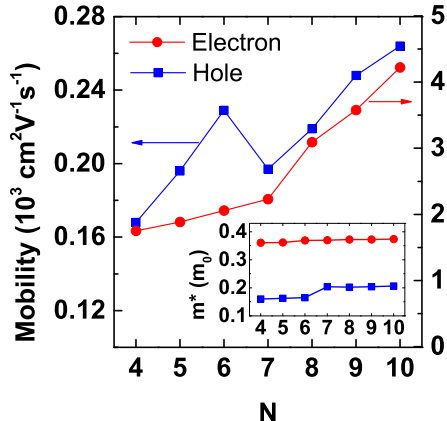


FIG. 6. (Color online) Carrier mobility for **b**-TiS<sub>3</sub> NRs. The inset shows the calculated effective mass  $m^*$  of electrons and holes for different ribbon widths.  $m_0$  is the mass of a free electron.

[47]. Neglecting polar scattering overestimates the carrier mobility. According to a recent work [48], the carrier mobility is overestimated by 100% for MoS<sub>2</sub> if only acoustic scattering is considered. In the present study, we limit ourselves to an order of magnitude estimate and to the trend of the mobility rather than providing precise values. By neglecting polar scattering we cannot provide very accurate results for the mobility; however, we can still give qualitatively satisfied results for orders of magnitude. For example, a previous study showed that the magnitude of mobility ( $\sim 100 \text{ cm}^2 \text{ V}^{-1} \text{ s}^{-1}$ ) of MoS<sub>2</sub> could be deduced by using Eqs. (1) and (2) [46].

The calculated mobilities for different **b**-TiS<sub>3</sub> NRs, as well as those for the 2D monolayer, are listed in Table II. We show the trend of the mobility with the ribbon width in Fig. 6. For a 2D TiS<sub>3</sub> sheet, our results are in good agreement with previous theoretical findings [22]. The electron (hole) mobility along the *b* direction is one order higher (lower) than that along the *a* direction. Moreover, the electron mobility along the *b* direction is as high as  $2.16 \times 10^4 \text{ cm}^2 \text{ V}^{-1} \text{ s}^{-1}$ , two orders higher than that of holes. This results from the larger effective mass and deformation potential of holes than of electrons. The **b**-TiS<sub>3</sub> NRs are all along the *b* direction. Table II shows that the discrepancy in the electron/hole mobility of the 2D monolayer also appears in these ribbons. For  $N = 4\text{--}10$ , the mobility of electrons in the ribbons varies from  $1.751 \times 10^3$  to  $4.222 \times 10^3 \text{ cm}^2 \text{ V}^{-1} \text{ s}^{-1}$ . The hole mobility is in the range of  $1.68 \times 10^2$  to  $2.64 \times 10^2 \text{ cm}^2 \text{ V}^{-1} \text{ s}^{-1}$ , one order lower than that of electrons. The effective mass of holes is about half of that of electrons, but holes have a much larger deformation potential, leading to their low mobility. As discussed above, the charge density of the VBM state has more components along the axial (*y*) direction than the CBM does; therefore, it is more sensitive to axial strain, and the deformation potential of holes is larger.

As shown in Fig. 6, generally, the mobility increases with the width of the ribbon. Compared with that of the infinite 2D sheet, the electron mobility in **b**-TiS<sub>3</sub> NRs is smaller. From monolayer to nanoribbon, the electron effective mass is almost unchanged, but there is a large increase (70%–100%) in the deformation potential. This explains the reduction of the electron mobility. Nevertheless, the electron mobility of

$\sim 10^3 \text{ cm}^2 \text{ V}^{-1} \text{ s}^{-1}$  in **b**-TiS<sub>3</sub> NRs is still considerable for TMCs. In contrast, the mobility of MoS<sub>2</sub> nanoribbons is only around  $200 \text{ cm}^2 \text{ V}^{-1} \text{ s}^{-1}$  [46]. Therefore, devices fabricated with **b**-TiS<sub>3</sub> NRs are expected to perform much better than those fabricated with MoS<sub>2</sub> nanoribbons. The presence of an edge reduces the electron mobility but enhances the hole mobility. The hole mobility in **b**-TiS<sub>3</sub> NRs is 2 to 3 times larger than that in a monolayer. Due to the strong edge effect, from monolayer to nanoribbon, the effective mass of the hole significantly decreases, which compensates the increase in deformation potential and leads to the higher mobility. In addition, from  $N = 6$  to  $N = 7$  there is a sudden decrease in hole mobility, which is mainly caused by the change in hole effective mass. As seen in the inset of Fig. 6, the hole effective mass is around  $0.16m_0$  for  $N \leq 6$  and around  $0.20m_0$  for  $N > 6$ . A larger effective mass leads to a smaller mobility.

It should be noted that Eqs. (1) and (2) assume an ideal parabolic band dispersion. It can be seen from Fig. 3(a) that the band dispersion of TiS<sub>3</sub> NRs around the CBM and VBM are close to parabolic dispersion. To further see whether such an approximation is valid, we did test calculations for a 6-**b**-TiS<sub>3</sub> NR following the method of Long *et al.* [45], who used the full band dispersion instead of the effective mass approximation. The calculated mobilities for electrons and holes were  $3.708 \times 10^3$  and  $0.352 \times 10^3 \text{ cm}^2 \text{ V}^{-1} \text{ s}^{-1}$ , respectively. On the other hand, using the effective mass approximation results in an electron mobility of  $2.057 \times 10^3 \text{ cm}^2 \text{ V}^{-1} \text{ s}^{-1}$  and a hole mobility of  $0.229 \times 10^3 \text{ cm}^2 \text{ V}^{-1} \text{ s}^{-1}$ , as listed in Table II. Thus, both methods lead to the same conclusion that the magnitudes of electron and hole mobilities are  $10^3 \text{ cm}^2 \text{ V}^{-1} \text{ s}^{-1}$  and  $10^2 \text{ cm}^2 \text{ V}^{-1} \text{ s}^{-1}$ , respectively. Our main concern was to provide an order of magnitude and the trend in the mobility rather than precise values, and therefore, the effective mass approximation is sufficient for the systems studied in the present work.

## VII. EDGE TERMINATION

Formation of one-dimensional structures of single-layer crystals results in the emergence of additional features such as edge states. It has been shown for many materials that termination of dangling bond states located at the edges can change the characteristics of the material drastically. In this section we investigate the effect of edge termination on the electronic and magnetic properties of **a**- and **b**-TiS<sub>3</sub> NRs. For the termination of ribbon edges we make use of hydrogenation. Compared to graphene nanoribbons, TiS<sub>3</sub> NRs are quite different due to their edge morphology. At each ribbon edge, while **a**-TiS<sub>3</sub> NRs have four edge atoms in the unit cell, **b**-TiS<sub>3</sub> NRs have two edge atoms. Among the various possible hydrogenation scenarios, we employ single hydrogen termination of each edge atom.

Our calculations reveal that upon hydrogenation of **a**-TiS<sub>3</sub> NR edges, metallic behavior of bare **a**-edged ribbons is still preserved. As shown in Fig. 7(a), compared with that of the bare-edge case, the overall electronic band dispersion of 8-**a**-TiS<sub>3</sub> NR is not affected significantly. However, the magnetic ground state of the structure is modified upon edge termination. As can be deduced from the enhanced splitting in spin-up (solid curves) and spin-down (dashed curves) bands,

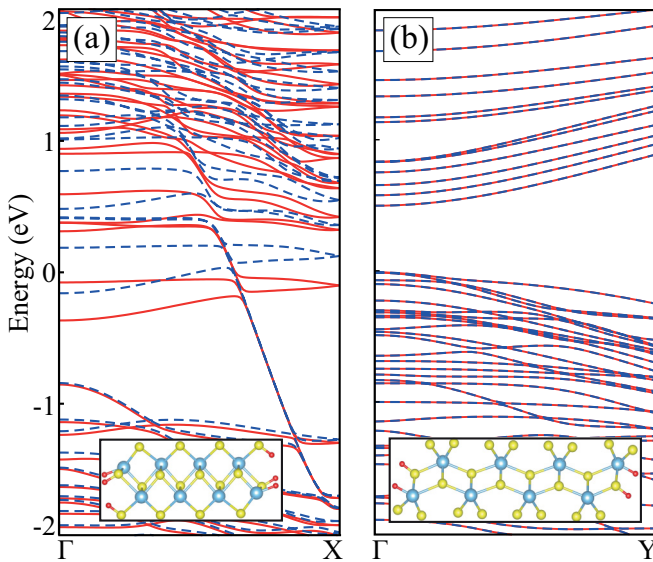


FIG. 7. (Color online) Band dispersions of (a) an 8-**a**-TiS<sub>3</sub> NR and (b) an 8-**b**-TiS<sub>3</sub> NR in which the edge atoms are passivated by hydrogen (red) atoms. The solid and dashed curves are spin-up and spin-down components. Insets show the side view of the edge structure.

hydrogenated ribbons possess a larger net magnetic moment in their ground state. For instance, in the case of 8-**a**-TiS<sub>3</sub> NR the total magnetic moment increases from  $0.3\mu_B$  to  $1.1\mu_B$  per unit cell. The robust metallic and ferromagnetic nature of **a**-TiS<sub>3</sub> NRs is an essential feature for spintronic device applications.

On the other hand, the situation is entirely different for **b**-TiS<sub>3</sub> NRs. Comparing Figs. 7(b) and 3(a), we see that the band gap of 8-**b**-TiS<sub>3</sub> NR increases due to edge termination. It increased from 0.32 to 0.51 eV. Moreover, although the VBM and the CBM points are still located at the  $\Gamma$  point, the band dispersion is significantly affected by the edge termination. It is also seen that similar to bare ribbons, hydrogen terminated **b**-TiS<sub>3</sub> NRs are nonmagnetic. The presence of a band gap in the electronic structure of **b**-TiS<sub>3</sub> NRs is important for their potential use in optoelectronic device applications.

## VIII. CONCLUSIONS

In summary, we investigated the electronic and mechanical properties of TiS<sub>3</sub> NRs by first-principles calculations. Our results reveal that **a**- and **b**-TiS<sub>3</sub> NRs have very different electronic characteristics and different mechanical responses to applied strain. While **a**-TiS<sub>3</sub> NRs show ferromagnetic metallic behavior, all the **b**-TiS<sub>3</sub> NRs have direct band gaps at the  $\Gamma$  point and are nonmagnetic. In contrast to nanoribbons of other single-layer materials such as graphene, the band gap is almost independent of the ribbon width. In addition, when tensile strain is applied, the band gap of **b**-TiS<sub>3</sub> NRs increases, and a direct-to-indirect band gap transition takes place. We showed that local strain in a **b**-TiS<sub>3</sub> NR creates a type-I band offset, which can induce carrier localization and a charge transport barrier. In addition going from an infinite 2D sheet to a nanoribbon, the electron (hole) mobility of TiS<sub>3</sub> is reduced (enhanced) as a consequence of the width-dependent deformation potential (effective mass). Finally, we showed that upon termination of the ribbon edges by hydrogen atoms, the **a**-TiS<sub>3</sub> NRs remain metallic and magnetic, but the band gap of **b**-TiS<sub>3</sub> NRs is increased. The robust metallic and ferromagnetic nature of **a**-NRs and the direct, width-independent, and strain-tunable band gap of **b**-NRs reveal the importance of TiS<sub>3</sub> NRs in various fields of nanotechnology.

## ACKNOWLEDGMENTS

This work was supported by the Flemish Science Foundation (FWO-VI) and the Methusalem foundation of the Flemish government. Computational resources were provided by TUBITAK ULAKBIM, the High Performance and Grid Computing Center (TR-Grid e-Infrastructure), and the HPC infrastructure of the University of Antwerp (CalcUA), a division of the Flemish Supercomputer Center (VSC), which is funded by the Hercules Foundation. H.S. is supported by a FWO Pegasus-Long Marie Curie Fellowship, and J.K. is supported by a FWO Pegasus-Short Marie Curie Fellowship. H.S. and R.T.S. acknowledge support from TUBITAK through Project No. 114F397.

- 
- [1] K. S. Novoselov, A. K. Geim, S. Morozov, D. Jiang, Y. Zhang, S. Dubonos, I. Grigorieva, and A. Firsov, *Science* **306**, 666 (2004).
  - [2] K. S. Novoselov, D. Jiang, F. Schedin, T. J. Booth, V. V. Khotkevich, S. V. Morozov, and A. K. Geim, *Proc. Natl. Acad. Sci. U.S.A.* **102**, 10451 (2005).
  - [3] P. Vogt, P. De Padova, C. Quaresima, J. Avila, E. Frantzeskakis, M. C. Asensio, A. Resta, B. Ealet, and G. Le Lay, *Phys. Rev. Lett.* **108**, 155501 (2012).
  - [4] E. Bianco, S. Butler, S. Jiang, O. D. Restrepo, W. Windl, and J. E. Goldberger, *ACS Nano* **7**, 4414 (2013).
  - [5] D. J. Late, B. Liu, H. S. S. R. Matte, C. N. R. Rao, and V. P. Dravid, *Adv. Funct. Mater.* **22**, 1894 (2012).
  - [6] L. Li, Y. Yu, G. J. Ye, Q. Ge, X. Ou, H. Wu, D. Feng, X. H. Chen, and Y. Zhang, *Nat. Nanotechnol.* **9**, 372 (2014).
  - [7] K. F. Mak, C. Lee, J. Hone, J. Shan, and T. F. Heinz, *Phys. Rev. Lett.* **105**, 136805 (2010).
  - [8] B. Radisavljevic, A. Radenovic, J. Brivio, V. Giacometti, and A. Kis, *Nat. Nanotechnol.* **6**, 147 (2011).
  - [9] A. Splendiani, L. Sun, Y. Zhang, T. Li, J. Kim, C.-Y. Chim, G. Galli, and F. Wang, *Nano Lett.* **10**, 1271 (2010).
  - [10] K. He, C. Poole, K. F. Mak, and J. Shan, *Nano Lett.* **13**, 2931 (2013).
  - [11] P. Johari and V. B. Shenoy, *ACS Nano* **6**, 5449 (2012).
  - [12] A. Ramasubramaniam, *Phys. Rev. B* **86**, 115409 (2012).
  - [13] T. Cao, G. Wang, W. Han, H. Ye, C. Zhu, J. Shi, Q. Niu, P. Tan, E. Wang, B. Liu, and J. Feng, *Nat. Commun.* **3**, 887 (2012).
  - [14] Z. Yin, H. Li, H. Li, L. Jiang, Y. Shi, Y. Sun, G. Lu, Q. Zhang, X. Chen, and H. Zhang, *ACS Nano* **6**, 74 (2012).

- [15] S. Tongay, J. Zhou, C. Ataca, K. Lo, T. S. Matthews, J. Li, J. C. Grossman, and J. Wu, *Nano Lett.* **12**, 5576 (2012).
- [16] S. Tongay, H. Sahin, C. Ko, A. Luce, W. Fan, K. Liu, J. Zhou, Y.-S. Huang, C.-H. Ho, J. Yan, D. F. Ogletree, S. Aloni, J. Ji, S. Li, J. Li, F. M. Peeters, and J. Wu, *Nat. Commun.* **5**, 3252 (2014).
- [17] S. Horzum, D. Cakir, J. Suh, S. Tongay, Y.-S. Huang, C.-H. Ho, J. Wu, H. Sahin, and F. M. Peeters, *Phys. Rev. B* **89**, 155433 (2014).
- [18] I. Ferrer, M. Maciá, V. Carcelén, J. Ares, and C. Sánchez, *Energy Procedia* **22**, 48 (2012).
- [19] I. Ferrer, J. Ares, J. Clamagirand, M. Barawi, and C. Sánchez, *Thin Solid Films* **535**, 398 (2013).
- [20] J. O. Island, M. Buscema, M. Barawi, J. M. Clamagirand, J. R. Ares, C. Sánchez, I. J. Ferrer, G. A. Steele, H. S. van der Zant, and A. Castellanos-Gomez, *Adv. Opt. Mater.* **2**, 641 (2014).
- [21] J. O. Island, M. Barawi, R. Biele, A. Almazán, J. M. Clamagirand, J. R. Ares, C. Sánchez, H. S. J. van der Zant, J. V. Álvarez, R. D'Agosta, I. J. Ferrer, and A. Castellanos-Gomez, *Adv. Mater.* **27**, 2595 (2015).
- [22] J. Dai and X. C. Zeng, *Angew. Chem. Int. Ed.* **54**, 7572 (2015).
- [23] Y. Jin, X. Li, and J. Yang, *Phys. Chem. Chem. Phys.* **17**, 18665 (2015).
- [24] F. Iyikanat, H. Sahin, R. T. Senger, and F. M. Peeters, *J. Phys. Chem. C* **119**, 10709 (2015).
- [25] Y. W. Son, M. L. Cohen, and S. G. Louie, *Phys. Rev. Lett.* **97**, 216803 (2006).
- [26] Y. Li, Z. Zhou, S. Zhang, and Z. Chen, *J. Am. Chem. Soc.* **130**, 16739 (2008).
- [27] H. Sahin, C. Ataca, and S. Ciraci, *Phys. Rev. B* **81**, 205417 (2010).
- [28] J. Kim, M. V. Fischetti, and S. Aboud, *Phys. Rev. B* **86**, 205323 (2012).
- [29] V. Tran and L. Yang, *Phys. Rev. B* **89**, 245407 (2014).
- [30] G. Kresse and J. Hafner, *Phys. Rev. B* **47**, 558 (1993).
- [31] G. Kresse and J. Furthmüller, *Phys. Rev. B* **54**, 11169 (1996).
- [32] P. E. Blöchl, *Phys. Rev. B* **50**, 17953 (1994).
- [33] J. P. Perdew, K. Burke, and M. Ernzerhof, *Phys. Rev. Lett.* **77**, 3865 (1996).
- [34] H. J. Monkhorst and J. D. Pack, *Phys. Rev. B* **13**, 5188 (1976).
- [35] J. Heyd, G. E. Scuseria, and M. Ernzerhof, *J. Chem. Phys.* **118**, 8207 (2003).
- [36] A. V. Kruckau, O. A. Vydróv, A. F. Izmaylov, and G. E. Scuseria, *J. Chem. Phys.* **125**, 224106 (2006).
- [37] P. Mori-Sánchez, A. J. Cohen, and W. Yang, *Phys. Rev. Lett.* **100**, 146401 (2008).
- [38] L. Brattas and A. Kjekshus, *Acta Chem. Scand.* **26**, 3441 (1972).
- [39] F. Güller, A. M. Llois, J. Goniakowski, and C. Noguera, *Phys. Rev. B* **91**, 075407 (2015).
- [40] S. Jun, *Phys. Rev. B* **78**, 073405 (2008).
- [41] J. Li and L.-W. Wang, *Phys. Rev. B* **72**, 125325 (2005).
- [42] J. Bardeen and W. Shockley, *Phys. Rev.* **80**, 72 (1950).
- [43] F. B. Beleznay, F. Bogar, and J. Ladik, *J. Chem. Phys.* **119**, 5690 (2003).
- [44] M. Long, L. Tang, D. Wang, L. Wang, and Z. Shuai, *J. Am. Chem. Soc.* **131**, 17728 (2009).
- [45] M. Long, L. Tang, D. Wang, Y. Li, and Z. Shuai, *ACS Nano* **5**, 2593 (2011).
- [46] Y. Cai, G. Zhang, and Y.-W. Zhang, *J. Am. Chem. Soc.* **136**, 6269 (2014).
- [47] N. Ma and D. Jena, *Phys. Rev. X* **4**, 011043 (2014).
- [48] K. Kaasbjerg, K. S. Thygesen, and K. W. Jacobsen, *Phys. Rev. B* **85**, 115317 (2012).